

Article

Study of Tensile and Compressive Behavior of ECO-Mg₉₇Gd₂Zn₁ Alloys Containing Long-Period Stacking Ordered Phase with Lamellar Structure

Gerardo Garcés ^{1,*}, Judit Medina ¹, Pablo Pérez ¹, Rafael Barea ², Hyunkyu Lim ³, Shae K. Kim ³, Emad Maawad ⁴, Norbert Schell ⁴ and Paloma Adeva ¹

- ¹ Department of Physical Metallurgy, CENIM-CSIC, Avenida Gregorio del Amo 8, 8040 Madrid, Spain; judit.medina@cenim.csic.es (J.M.); zubiaur@cenim.csic.es (P.P.); adeva@cenim.csic.es (P.A.)
- ² Department of Industrial Engineering, Universidad Nebrija, Campus Madrid-Princesa, Santacruz de Marcenado, 27, 28015 Madrid, Spain; rbarea@nebrija.es
- ³ Casting Research, Korea Institute of Industrial Technology (KITECH), 7-47 Songdo-dong, Yeonsu-gu, Incheon 406-840, Republic of Korea; hklm@kitech.re.kr (H.L.); shae@kitech.re.kr (S.K.K.)
- ⁴ Institute of Materials Physics, Helmholtz-Zentrum Geesthacht, Max-Planck-Str. 1, 21502 Geesthacht, Germany; emad.maawad@hereon.de (E.M.); norbert.schell@hzg.de (N.S.)
- * Correspondence: ggarcés@cenim.csic.es; +34-915538900

Abstract: A suitable heat treatment in the Mg₉₇Gd₂Zn₁ (at.%) alloy in the as-cast condition results, after extrusion at high temperature, in a two-phase lamellar microstructure consisting of magnesium grains with thin lamellar shape precipitates and long fibers of the 14H-Long-Period Stacking Ordered (LPSO) phase elongated in the extrusion direction. The magnesium matrix is not fully recrystallized and highly oriented coarse non-dynamically recrystallized (non-DRXed) grains (17% volume fraction) elongated along the extrusion direction remain in the material. The deformation mechanisms of the extruded alloy have been studied measuring the evolution of the internal strains during in situ tension and compression tests using synchrotron diffraction radiation. The data demonstrate that the macroscopic yield stress is governed by the activation of the basal slip system in the randomly oriented equiaxed dynamic recrystallized (DRXed) grains. Non-DRXed grains, due to their strong texture, are favored oriented for the activation of tensile twinning. However, the presence of lamellar-shape precipitates strongly delays the propagation of lenticular thin twins through these highly oriented grains and they have no effect on the onset of the plastic deformation. Therefore, the tension–compression asymmetry is low since the plasticity mechanism is independent of the stress mode.

Keywords: magnesium alloys; mechanical properties; synchrotron radiation diffraction; long-period stacking ordered structures



Citation: Garcés, G.; Medina, J.; Pérez, P.; Barea, R.; Lim, H.; Kim, S.K.; Maawad, E.; Schell, N.; Adeva, P. Study of Tensile and Compressive Behavior of ECO-Mg₉₇Gd₂Zn₁ Alloys Containing Long-Period Stacking Ordered Phase with Lamellar Structure. *Metals* **2024**, *14*, 530. <https://doi.org/10.3390/met14050530>

Academic Editor: Qinghuan Huo

Received: 4 April 2024
Revised: 22 April 2024
Accepted: 23 April 2024
Published: 30 April 2024



Copyright: © 2024 by the authors. Licensee MDPI, Basel, Switzerland. This article is an open access article distributed under the terms and conditions of the Creative Commons Attribution (CC BY) license (<https://creativecommons.org/licenses/by/4.0/>).

1. Introduction

Mg-Rare earth (RE)-Zn alloys containing Long-Period Stacking Ordered (LPSO) phases exhibit high mechanical strength with substantial ductility [1–4]. Two types of these alloys can be distinguished depending on the presence or absence of the LPSO-phase in the as-cast condition. According to the RE elements added, these alloys can be referred to as Type I and Type II. Type I corresponds to Mg-(Y, Dy, Ho, Er, Tm)-Zn alloys in which the LPSO-phase is formed during the casting process [5–10]. In the case of Mg-(Gd, Tb, . . .)-Zn alloys, referred to as Type II, the LPSO-phase does not appear in the as-cast condition and a subsequent high-temperature thermal treatment is required to develop it [11–18]. After a solution treatment, a hardness peak can be reached by ageing the material at low temperatures. Yamasaki et al. [13] reported, in the Mg₉₇Gd₂Zn₁ (at.%) alloy, the formation during isothermal ageing of stacking faults and lamellar 14H phase at intermediate and high temperatures (300–500 °C), while intermetallic β' (orthor, Mg₇Gd [19]), β₁ (fcc, Mg₅Gd)

and β (fcc, Mg_5Gd) phases formed at low temperatures (~ 200 °C). On the other hand, Nie et al. [14] reported that the peak aged condition in $\text{Mg}_{98.6}\text{Gd}_1\text{Zn}_{0.4}$ (at.%) is caused by the formation of lamellar γ'' (ordered hexagonal structure, $P6\ 2m$) and γ' (disordered hexagonal structure, $P\bar{3}m1$). Since lamellar-shape precipitates are located parallel to the basal plane, these precipitates are considered to be ineffective obstacles to the motion of $\langle a \rangle$ dislocations along the basal plane. Nevertheless, a significantly low activity of the basal slip system in the Mg matrix in between LPSO lamellae, when interlamellar space is below 20 nm, has been also reported [20]. The high concentration of solute atoms near LPSO lamellae provides a strong solute strengthening effect. On the other hand, tensile twinning is also an important deformation system in magnesium alloys, especially in those alloys with intense texture. Lamellar-shape precipitates offer little resistance to the tensile twinning deformation mode [16], although they are effective in temporally delaying the coalescence twinning step [16,18,21]. Thus, microcracks can be initially nucleated along the (LPSO-phase/lamellar γ' phase)/ α -Mg matrix interfaces, and a significant stress dissipation is induced by mutual interactions between the tensile twinning and the kinking of the lamellar γ' phase, leading to an increase in fracture toughness K_{Ic} [22]. At high temperatures, the presence of lamellar γ' phase is an important obstacle to non-basal slip systems and it creates nucleation sites for extremely fine DRXed grains [23,24].

The hexagonal close-packed lattice of magnesium, with a limited number of active deformation systems, promotes the formation of a strong crystallographic texture when the alloy is thermomechanically processed, inducing the tension–compression yield asymmetry phenomenon. The mechanical asymmetry of magnesium alloys has been widely investigated, since it is an important factor limiting their industrial applications [25–29]. The tension–compression asymmetry in magnesium alloys containing LPSO-phases depends on the processing route and the microstructure [30]. Geng et al. [16] studied the influence of lamellar-shape precipitates on the tension–compression asymmetry in an extruded Mg-Gd-Zn alloy. Due to the weak texture generated during the full recrystallization process, the alloy showed negligible yield stress asymmetry. Yang et al. [18] also reported negligible yield stress asymmetry in a $\text{Mg}_{97.3}\text{Gd}_{2.1}\text{Zn}_{0.6}$ alloy characterized by highly oriented non-recrystallized grains with a high density of thin LPSO plates within the magnesium grains. It is expected that lamellar-shape precipitates could enhance dynamic recrystallization, minimizing the presence of non-DRXed grains. The study will be carried out through the measurement of the internal strains obtained using synchrotron radiation diffraction during in situ tensile and compressive tests.

2. Materials and Methods

Magnesium alloys with composition $\text{Mg}_{97}\text{Gd}_2\text{Zn}_1$ (at.%) were cast using an Environment Conscious (ECO) process, with the addition of 0.3 wt.% of CaO. The cast billet was thermally treated (TT condition) at 520 °C for 8 h while buried in MgO sand to minimize alloy oxidation. The cooling of the billets was carried out inside the furnace at 10 °Cmin⁻¹. The billet was machined at a 41 mm diameter and then it was extruded at an extrusion temperature of 350 °C, an extrusion rate of 0.5 mms⁻¹ and an extrusion ratio of 18:1.

Microstructural characterization of the alloys was carried out by optical microscopy (OM) and scanning and transmission electron microscopy (SEM (JEOL-JSM 6500F, JEOL-JSM 6500F, JEOL, Tokyo, Japan and Hitachi S4800J, Hitachi High-Tech Corporation, Ibaraki, Japan) and TEM (JEOL JEM 2010, JEOL, Tokyo, Japan), respectively). Samples for SEM observation were prepared by mechanical polishing using colloidal silica. Samples were analyzed at an operating voltage of 15 kV in both SEMs. Volume fractions of each alloy constituent (LPSO phase, magnesium DRXed grains and magnesium non-DRXed grains) were evaluated as follows. Firstly, the volume fraction of the LPSO phase was evaluated in the polished sample using the Fiji Image J software 2.9.0 (LOCI, University of Wisconsin, Madison, WI, USA) [31]. The backscattered SEM image clearly differentiates the LPSO phase due to its higher gadolinium and zinc concentrations with respect to the magnesium phase. The volume fractions of the DRXed and non-DRXed grains were evaluated in

the extruded sample after etching using OM. In this condition, the LPSO-phase and non-DRXed grains had similar aspects. Therefore, the volume fraction of DRXed grains was also evaluated using again Fiji Image J software. The volume fraction of the non-DRXed grains was balanced with the other two constituents. The grain size was measured by quantitative image analysis.

TEM specimens of deformed samples were prepared by electrolytic polishing using a reactive mixture of 5.3 g lithium chloride, 11.2 g magnesium perchlorate, 500 mL methanol and 100 mL butoxy-ethanol at $-50\text{ }^{\circ}\text{C}$ and 50 V.

The crystallographic texture of the alloy was evaluated using the Electron Backscattered Diffraction (EBSD) technique and the Rietveld analysis of the synchrotron diffraction patterns. Specimens for EBSD measurements were finally etched using a solution of 7 mL acetic acid, 3 mL nitric acid, 30 mL of ethanol and 10 mL of water. EBSD acquisition was carried out in a direction perpendicular to the extrusion direction and the data were recorded and analyzed using Channel 5 software (Oxford Instruments, Abingdon, Oxfordshire, UK).

Synchrotron radiation diffraction was carried out during in situ tension and compression tests at the P07B-HEMS beamline of PETRA III, at the Deutsches Elektronen-Synchrotron (DESY) (Hamburg, Germany). Cylindrical samples of diameter 5 mm and length 25 mm and cylinders of diameter 5 mm and length 10 mm were used in tension and compression, respectively. In both cases samples were machined along the extrusion direction and tested at a strain rate of 10^{-4} s^{-1} at room temperature. Samples were deformed in tension and compression in a tensile rig at an initial strain rate of 10^{-4} s^{-1} . The diffraction patterns were recorded using an exposure time of 0.5 s by a Perkin-Elmer XRD 1622 flat-panel detector (Perkin-Elmer, Waltham, MA, USA) with an array of 20.48^2 pixels, and an effective pixel size of $200 \times 200\text{ }\mu\text{m}^2$. The beam energy was 87 keV, corresponding to a wavelength of 0.014 nm. LaB6 was used as a reference to calibrate the acquired diffraction spectra. The detector-to-sample distance was set to 1637 mm.

Conventional line profiles were obtained by azimuthal integration of the Debye-Scherrer rings. The synchrotron radiation beam was positioned at the center of the sample, with the gauge volume defined approximately by the beam section ($0.8 \times 0.8\text{ mm}^2$) and the cylinder diameter. The elastic strain for each orientation can be calculated by the shift in the position of the diffraction peak:

$$\varepsilon_{hkl} = \frac{d_{hkl} - d_{0,hkl}}{d_{0,hkl}} \quad (1)$$

where d_{hkl} and $d_{0,hkl}$ are the planar spacing of the hkl plane in the stressed and stress-free crystal. The lattice spacing and the diffraction angle θ are related through Bragg's law.

The macroscopic texture was evaluated by Rietveld texture analysis using MAUD software (Luca Lutterotti, University of Trento, Italy) [32,33]. The 2D detector image is converted to a set of diffraction patterns using the Image J plugin in the software (LOCI, University of Wisconsin, WI, USA) [34,35], fitting the α -Mg (P63/mmc) and LPSO-14H (P63/mmc) [36]. The best fit to the experimental data was achieved using the E-WIMV algorithm with 5° resolution. This procedure was repeated within the compression test, obtaining the evolution of the texture as a function of the compressive strain. From the (0002) pole figure, the volume fraction of twins can be calculated following the procedure reported by Agnew et al. [37], given by

$$f_{tw} = \int_{\varphi=0}^{\varphi \approx 57^{\circ}} [I(\varphi) - I_0] \sin \varphi \, d\varphi \quad (2)$$

where φ is the angle of tilt between the (0002) poles and the compression axis and $I(\varphi)$ is the intensity at that tilt angle φ .

3. Results

The microstructure of the alloy in the as-cast condition, shown in Figure 1a, is characterized by the coexistence of the magnesium matrix (grey phase) with the intermetallic Mg_3Gd phase (white phase) [13]. The magnesium phase around the intermetallic phase shows a contrast provoked by an increase of the gadolinium solid solution in the magnesium phase. After thermal treatment, the microstructure changes drastically (Figure 1b). On one hand, the Mg_3Gd phase transforms into the LPSO-phase with composition $Mg_{29}Gd_{10}Zn_{0.2}Ca$ (wt.%). On the other hand, the precipitation of fine lamellae inside the Mg grains takes place (Figure 1c). The volume fraction of the LPSO phase is 17%. After extrusion at 350 °C, coarse LPSO-phase is deformed and elongated along the extrusion direction (Figure 1d).

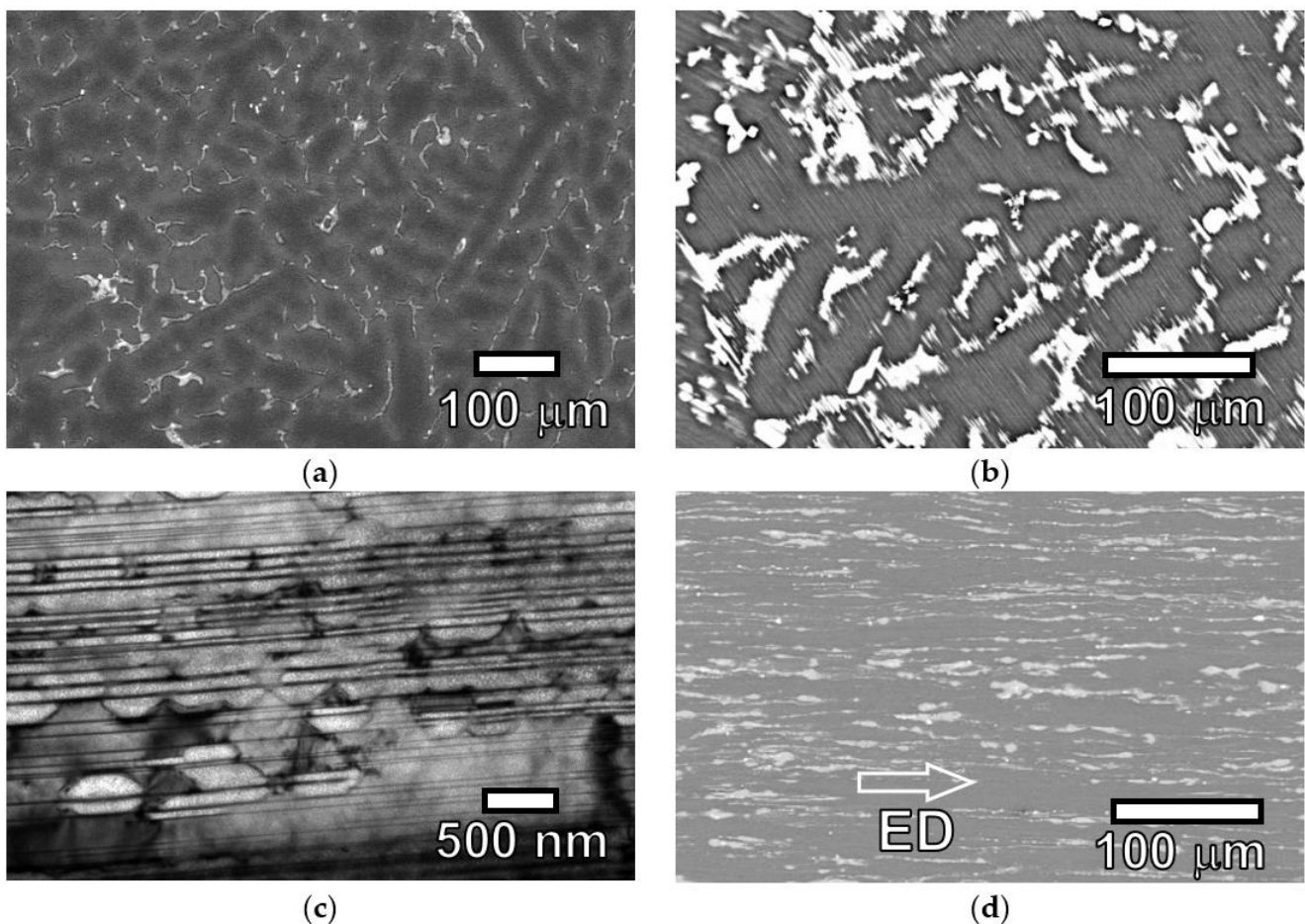


Figure 1. (a) Microstructure of the cast ECO- $Mg_{97}Gd_2Zn_1$ alloy. (b) Microstructure of the cast ECO- $Mg_{97}Gd_2Zn_1$ alloy after the thermal treatment, showing the lamellar structure in the magnesium phase. (c) Bright field image of the magnesium phase at the zone axis $B = [11\bar{2}0]$. (d) Microstructure of the extruded ECO- $Mg_{97}Gd_2Zn_1$ alloy along the extrusion direction (ED).

The grain structure after extrusion is shown in the orientation image maps (OIMs) of Figure 2a,b. The material is not completely recrystallized and the microstructure exhibits dynamic recrystallized (DRXed) grains with an average grain size of 1 μm (Figure 3) and non-dynamic recrystallized (non-DRXed) grains elongated along the extrusion direction, with a longer dimension of 300–400 μm . The volume fractions of fine DRXed and coarse elongated non-DRXed grains are 64 and 19%, respectively. DRXed grains are randomly oriented but the elongated, non-DRXed grains are highly oriented, with their basal plane parallel to the extrusion direction (grain A in Figure 2a), as observed in the (0002) pole figure of Figure 2c.

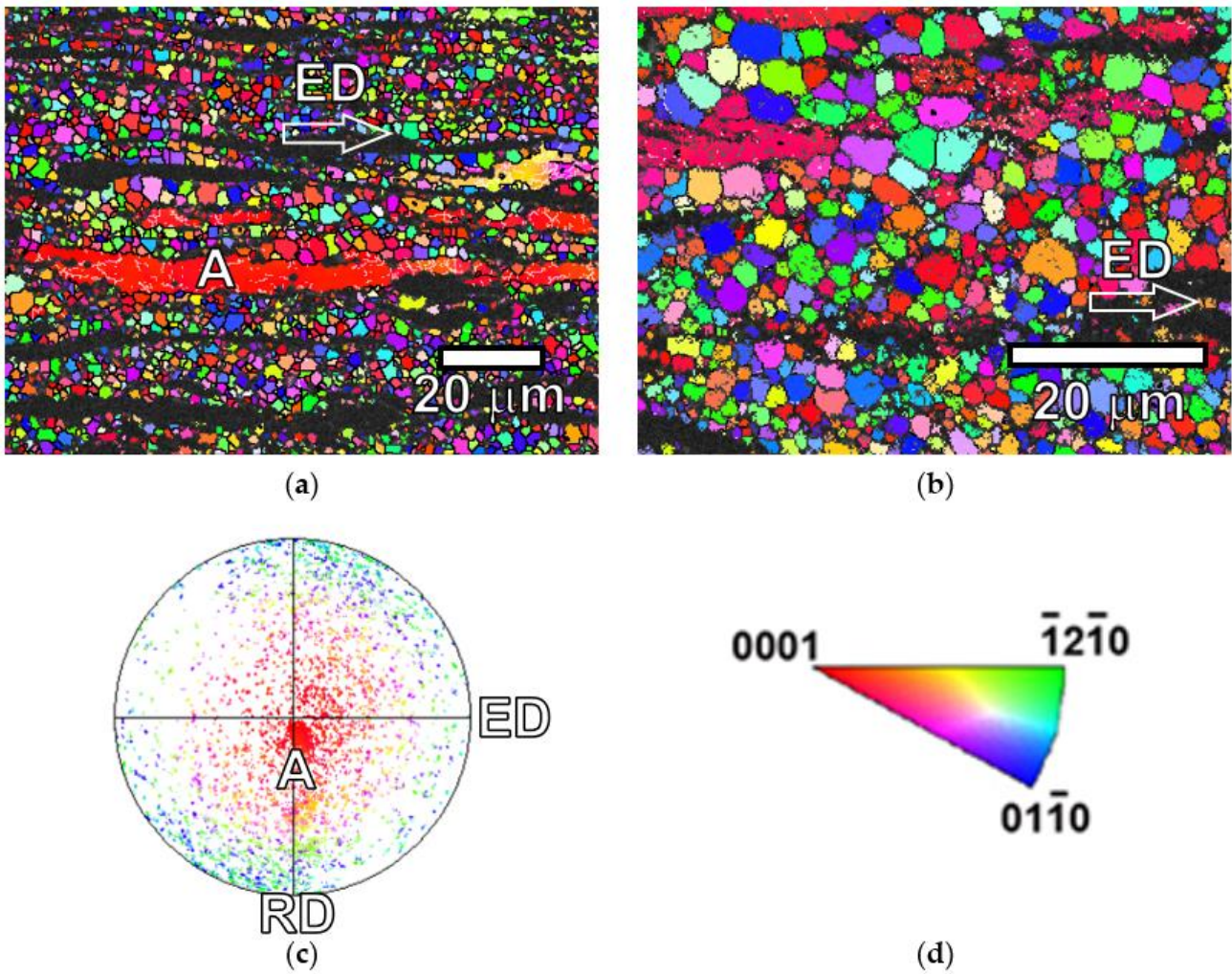


Figure 2. (a) Orientation image maps (OIMs) along the extrusion direction of the extruded ECO-Mg₉₇Gd₂Zn₁ alloy. (b) Detail of fine DRXed grains. (c) {0002} pole figure corresponding to EBSD map of (a). Red-orange intense accumulation in the radial direction comes from the non-DRXed grains (grain A). (d) IPF color key.

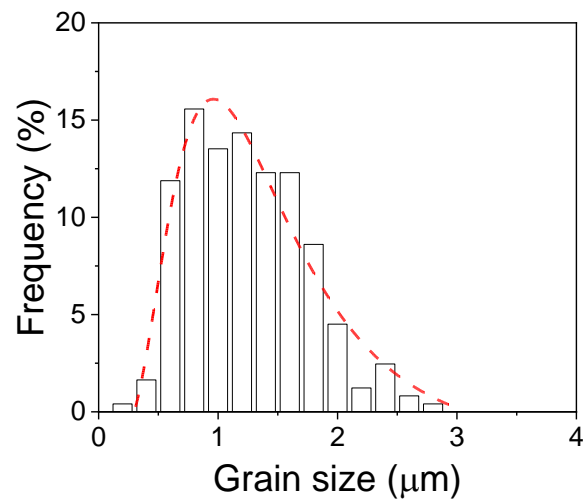


Figure 3. Grain histogram of DRXed grains.

The macroscopic texture was also evaluated using Rietveld texture analysis of the diffraction pattern obtained from the Debye–Scherrer diffracted rings. Figure 4 shows the Debye–Scherrer rings obtained before tension or compression tests for the extruded $\text{Mg}_{97}\text{Gd}_2\text{Zn}_1$ alloy (Figure 4a), as well as a detail of the innermost ring, corresponding to the (0002) diffracted ring of the 14H-LPSO phase. The intensity of each diffraction ring changes along the azimuthal angle due to the crystallographic texture of the magnesium and LPSO phases. Figure 4b shows the axial and radial diffraction pattern obtained from the integration of Figure 4a. In this plot, the different intensity of each diffraction peak corroborates the development of a crystallographic texture during the extrusion process. It is important to point out the presence of a strong diffraction peak in the radial direction at 0.45° , corresponding to the 0002-diffraction peak of the 14H-LPSO phase. In the axial direction, the most intense diffraction peak due to the magnesium phase corresponds to the $(10\bar{1}0)$ plane, which is perpendicular to the extrusion direction.

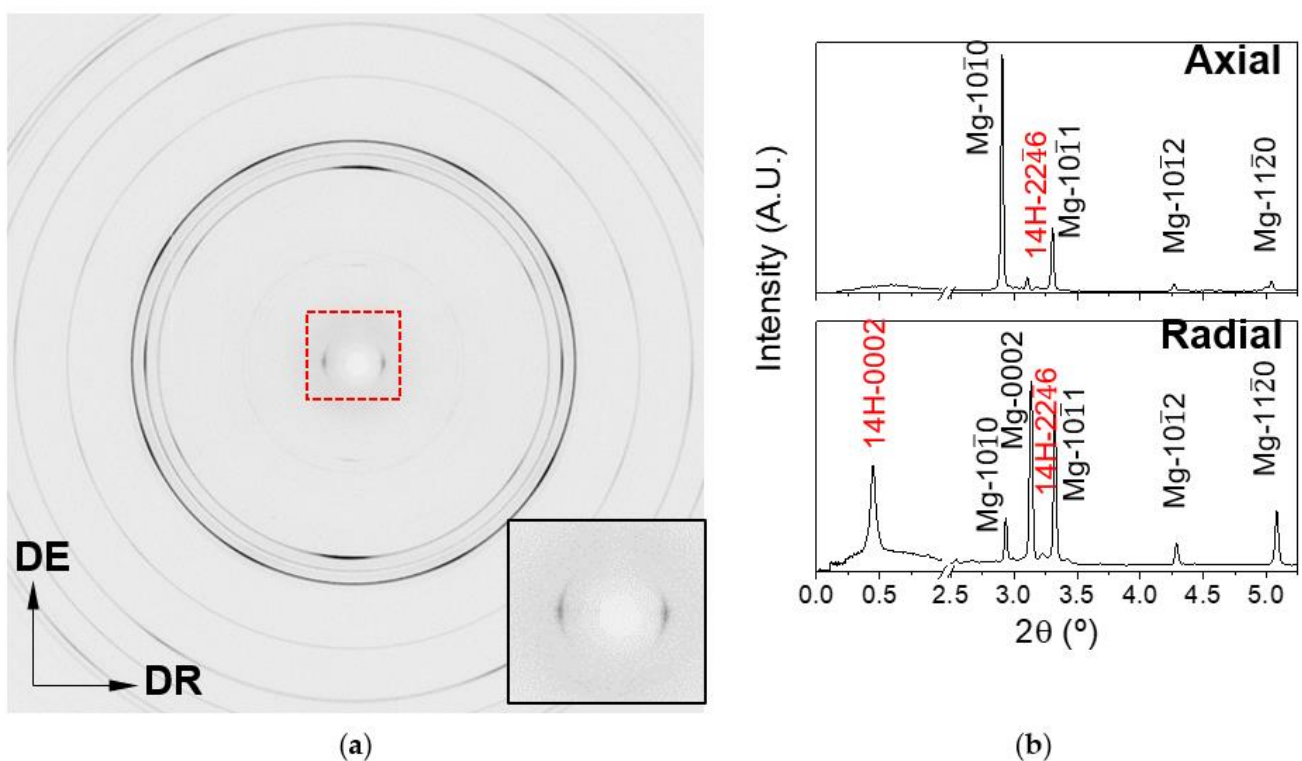


Figure 4. (a) Synchrotron radiation diffraction pattern recorded on the 2D flat-panel detector before the tension and compression tests. Detail of the innermost ring corresponding to the (0002) diffracted ring of the 14H-LPSO phase. (b) Axial and radial diffracted pattern integrated from (a).

Rietveld fitting of diffraction patterns in the axial, 45° between axial/radial direction and radial direction has been performed for the alloy in the as-extruded condition, assuming the presence of α -Mg and 14H-LPSO-phase (see Figure 5a–c). The pole figures obtained from the Rietveld texture analysis are presented in Figure 5d–f for the magnesium phase ($\{10\bar{1}0\}$ and (0002) pole figures) and LPSO-phase ((00014) pole figure).

Figure 6a–e show the microstructure using TEM of the non-DRXed grains, DRXed grains and short fibers of LPSO-phase, respectively. Non-DRXed grains (Figure 6a) are highly deformed due to the accumulation of a high dislocation density. Even more, subgrains limited by low angle grain boundaries are observed within these grains (see white arrow in Figure 6a). Within these grains, a lamellar structure is still observed, as found for the TT condition. However, the thin γ lamellar precipitates, about 10–20 nm in thickness, become coarser than those seen in the TT alloy (Figure 6b). In any case, thin precipitates of several nm are still placed in the basal plane. These precipitates are coherent with the

magnesium matrix and generate diffuse streaks along the $[0002]$ direction in the SAED pattern of Figure 6c.

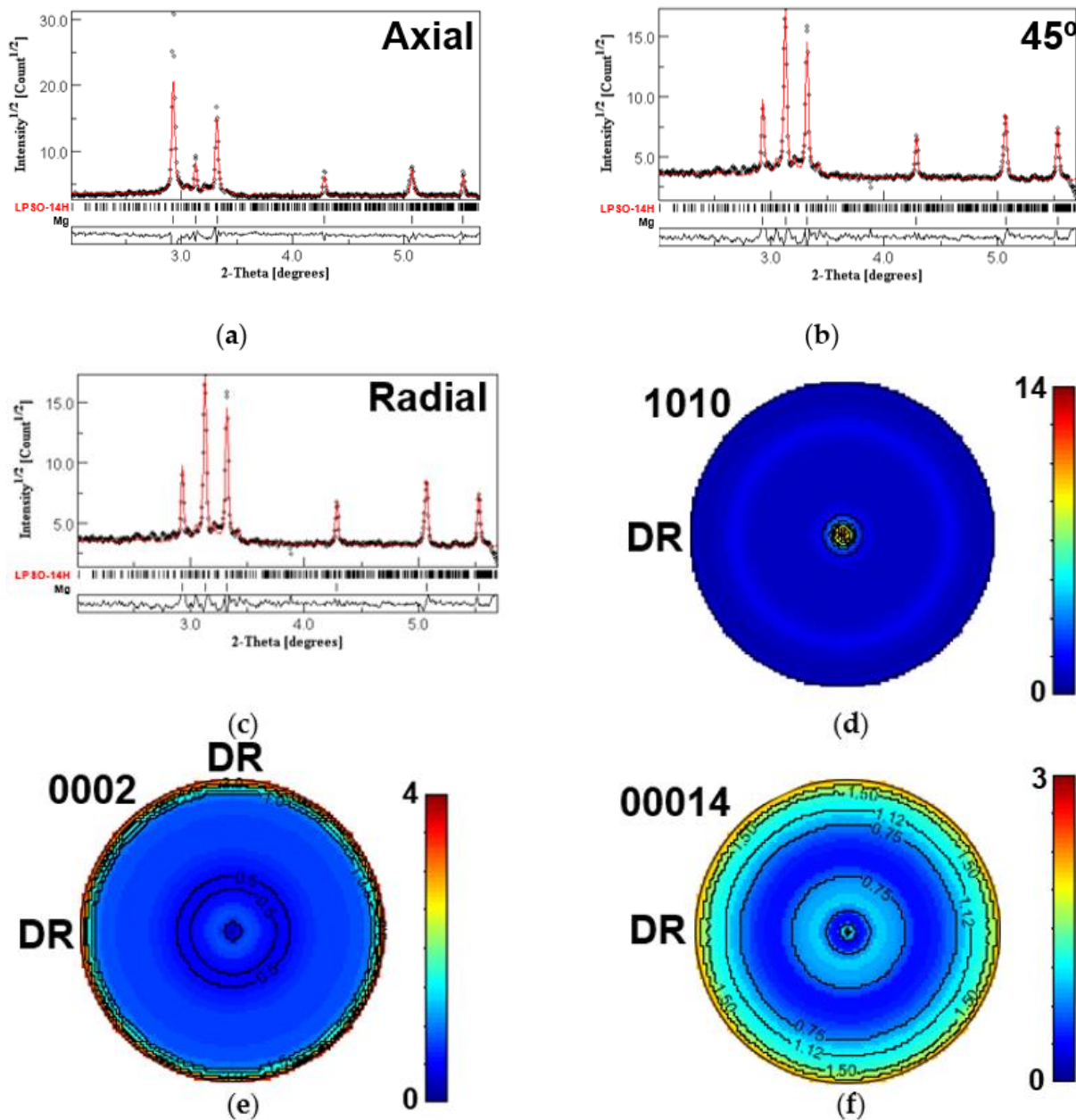


Figure 5. Rietveld analysis of diffraction patterns of extruded $Mg_{97}Gd_2Zn_1$ alloy: (a) axial, (b) 45° and (c) radial directions. (d) $\{0002\}$ and (e) $\{10\bar{1}0\}$ pole figures obtained from the magnesium phase and (f) $\{00014\}$ pole figure from the 14H-LPSO phase.

Figure 6d shows a bright field image of DRXed grains. Thin basal precipitates are equally observed within these grains. When thin precipitates are tilted, a Moiré structure (white arrow in Figure 6d) reveals that they are planar defects, I_2 stacking faults, generated by the formation of Shockley partial dislocations. It is important to point out that this structure is not homogeneous over the entire grain.

Finally, Figure 6e–g show bright field images of the LPSO-phase and its corresponding SAED pattern at the zone axis $B = [11\bar{2}0]$. As found in the non-DRXed grains, the LPSO-phase is highly deformed. The thickness of the LPSO-phase fiber is around $1 \mu m$. Inside

the LPSO-phase, a fringe structure with a spacing of about 1.8 nm along the c direction at the zone axis $B = [11\bar{2}0]$ is measured, corroborating the formation of the 14H structure [38].

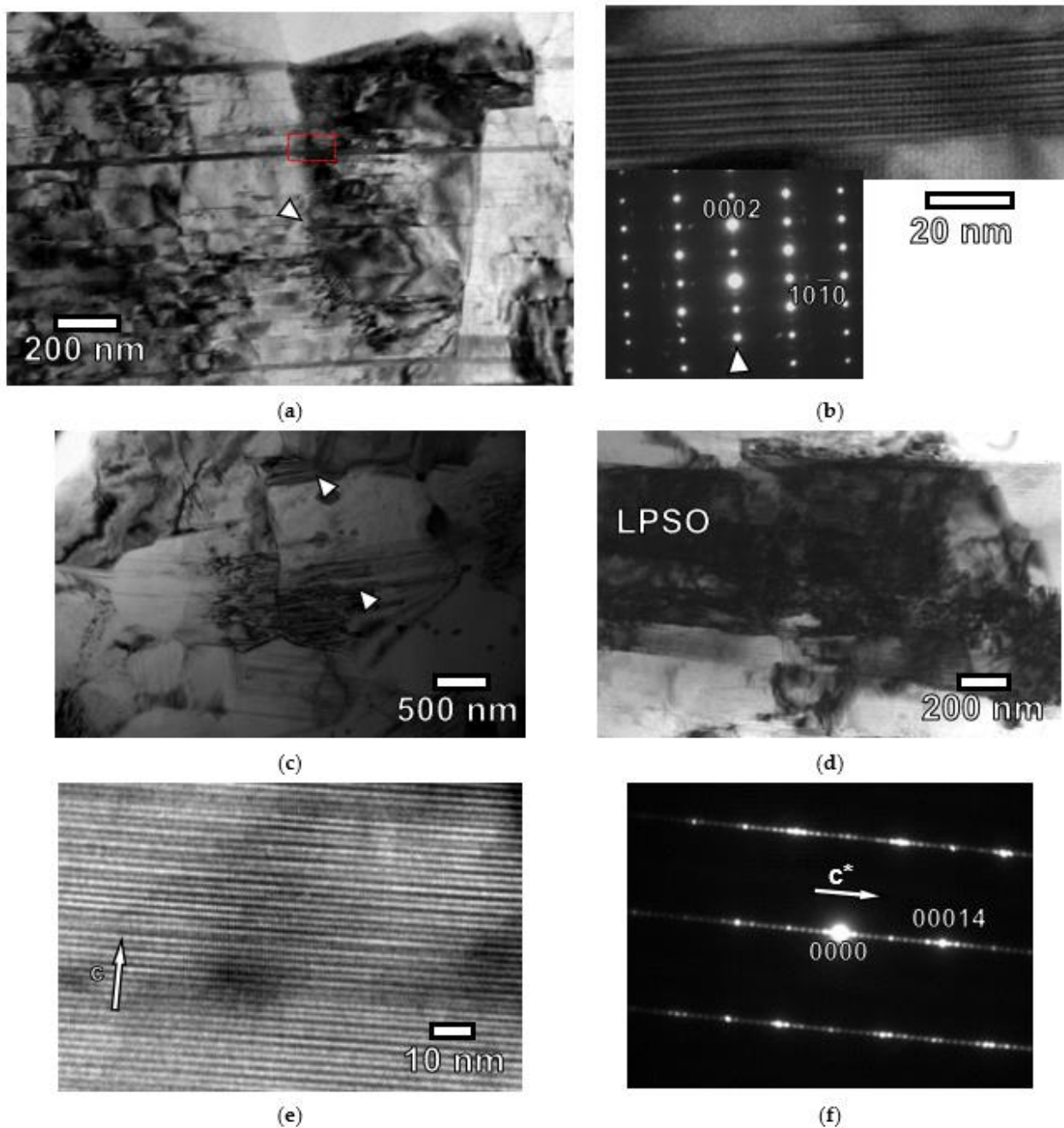


Figure 6. (a) Bright field image of a non-DRXed grain at the zone axis $B = [11\bar{2}0]$. (b) Detail of (a) corresponding to the 14H-LPSO lamellar structure and SAED pattern of the non-DRXed grain shown at the zone axis $B = [11\bar{2}0]$. (c) Bright field image of the DRXed grains. (d) Bright field image of the LPSO phase at the zone axis $B = [11\bar{2}0]$. (e) Detail of the LPSO phase shown in (d) with $g = (0002)$. (f) SAED pattern of the LPSO phase at the zone axis $B = [11\bar{2}0]$. The image is rotated 90° with respect to (e).

Tensile and compressive curves obtained during the in situ experiments in the beam-line for the extruded $Mg_{97}Gd_2Zn_1$ alloy are shown in Figure 7. The beginnings of the curves for both stress modes seem similar, at least until the point of 3% plastic strain. The yield stress is around 300 MPa in both cases. In compression, the sample was deformed to

the point of 10% plastic deformation. The curve exhibits a slightly sigmoidal or “S-type” concave shape, indicative of $\{10\bar{1}2\}\langle 10\bar{1}1\rangle$ extension twinning activation. In any case, it was found that the material flows plastically at stresses slightly higher than those seen under tensile loading.

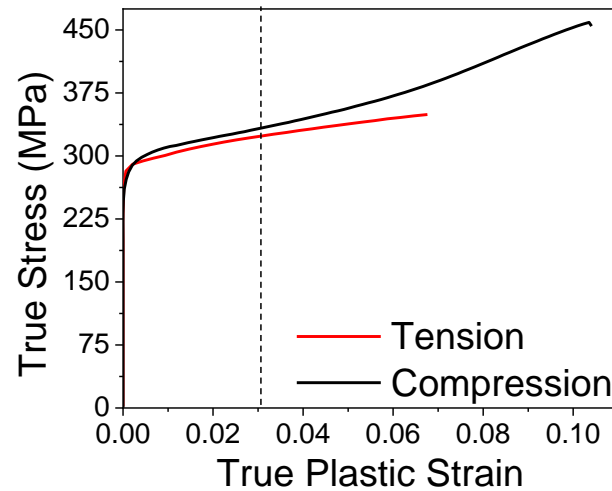


Figure 7. Tensile and compressive true stress–true strain curves for the extruded ECO-Mg₉₇Gd₂Zn₁ alloy obtained during the in situ experiments in the beamline.

The evolution of the elastic strains obtained from Equation (1) corresponding to the $\{10\bar{1}0\}$, $\{0002\}$, $\{10\bar{1}1\}$, $\{10\bar{1}2\}$ and $\{11\bar{2}0\}$ diffraction peaks for the magnesium phase and $\{42\bar{2}6\}$ diffraction peak for the 14H-LPSO are plotted in Figure 8 for tension and compression tests, respectively. The tensile and compressive stress–strain curves obtained during the in situ diffraction experiment are also plotted in Figure 8a,b in order to correlate the evolution of the internal elastic strains and the macroscopic elasto-plastic behavior. The evolution of internal strains in the axial and radial directions are complementary. Therefore, the result described is focused on the internal strains in the axial direction due to their larger changes.

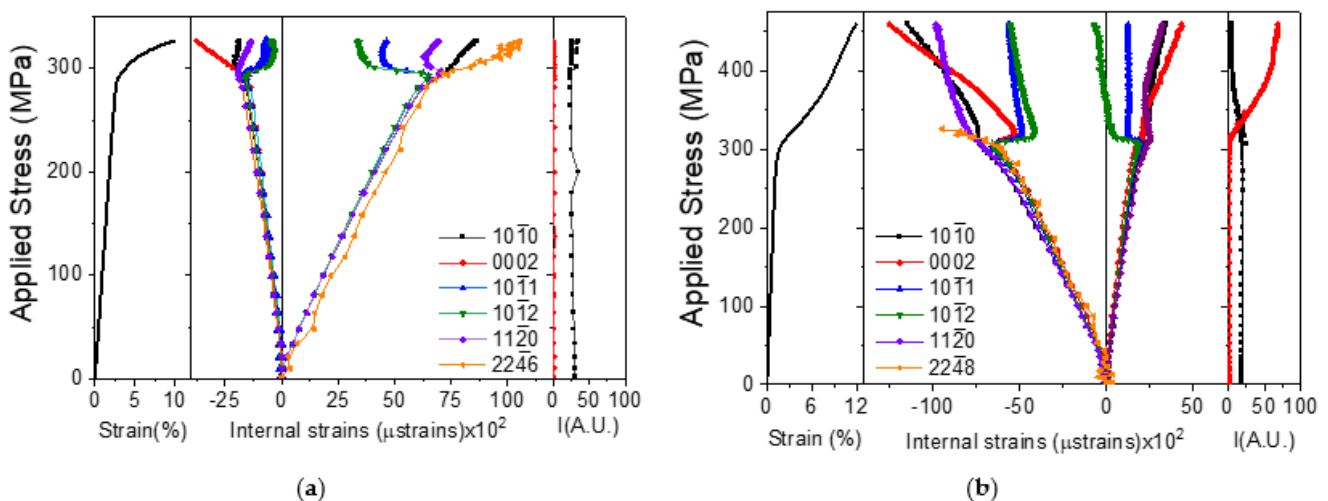


Figure 8. (a) Tensile and (b) compressive macroscopic stress–strain curves of the ECO-Mg₉₇Gd₂Zn₁ alloy obtained during the in situ experiments. Axial and radial internal strains as a function of the applied stress during in situ (a) tension and (b) compression tests at room temperature. Evolution of the integrated intensity of the $\{10\bar{1}0\}$ and $\{0002\}$ diffraction peaks during (a) tensile and (b) compressive tests.

In tension, the macroscopic yield stress, measured at 0.2% of the plastic deformation, was around 292 MPa. Below this stress level, the evolution of the elastic strains for all analyzed diffraction peaks of the magnesium phase as a function of the applied stress is completely linear. Magnesium alloys are elastically isotropic and no differences in the elastic strains for different orientations have been reported in the elastic regime [39]. The slope of the elastic strains corresponding to the diffraction peak of the LPSO-phase evolves in a similar way. The Young modulus of each family of grains was estimated through the slope of the elastic strains in the elastic regime, resulting in a value of 43 GPa. Above 300 MPa, elastic strains of $\{10\bar{1}1\}$ and $\{10\bar{1}2\}$ planes perpendicular to the tensile axis deviate from the straight line, decreasing the elastic internal strain from 6617 μ strains at 293 MPa to 4584 μ strains and 3560 μ strains at 312 MPa, for $\{10\bar{1}1\}$ and $\{10\bar{1}2\}$ diffraction peaks, respectively. After this stress was applied, the elastic strains were constant, which implies that these grains deform plastically.

The decrease in the elastic strains of grains oriented with the $\{10\bar{1}1\}$ and $\{10\bar{1}2\}$ grains perpendicular to the tensile axis is accompanied by an increase in the elastic strains for the grains oriented with their prismatic $\{10\bar{1}0\}$ planes perpendicular to the tensile axis and for the 14H LPSO-phase. It is interesting to point out that elastic strain of the LPSO phase increases faster (as a function of the applied stress) than the prismatic orientation.

The behavior of the elastic strains of grains oriented with their $\{11\bar{2}0\}$ planes perpendicular to the tensile axis is complex and presents three different stages. After yielding, and up to 298 MPa, the elastic strain increases, following a behavior similar to that of the elastic strains for the $\{10\bar{1}0\}$ diffraction peak. Then, the elastic strain decreases following a behavior similar to that of the elastic strains of $\{10\bar{1}1\}$ and $\{10\bar{1}2\}$ diffraction peaks, from 7170 μ strains at 298 MPa to 6359 μ strain at 312 MPa. Then, elastic strain remains almost constant, which implies that grains oriented with $\{11\bar{2}0\}$ planes perpendicular to the tensile axis deform plastically. Finally, the $\{0002\}$ diffraction peak cannot be accurately fitted in the plastic regime because of its low intensity, as observed in Figure 8a.

In compression, the macroscopic yield stress was around 302 MPa. Below this level of stress, the evolution of the elastic strains as a function of the applied stress exhibits a linear elastic behavior, as found in tension tests. The slope is identical for all analyzed diffraction peaks for the magnesium phase, with a Young modulus of 47 GPa.

After yielding at 300 MPa, a value equal to that for the tensile test, the elastic strain of the $\{10\bar{1}1\}$ and $\{10\bar{1}2\}$ planes perpendicular to the compression axis deviate from the straight line, decreasing (in absolute values) the elastic internal strain from 6620 μ strains at 302 MPa to 4913 μ strains and 4119 μ strains at 320 MPa, for $\{10\bar{1}1\}$ and $\{10\bar{1}2\}$ diffraction peaks, respectively. After this applied stress, the elastic strains are again constant, which implies that these grains deform plastically.

During the compression test, the elastic strain of the grains oriented with $\{10\bar{1}0\}$ planes perpendicular to the compression axis follows the same linear slope observed in the elastic regime. On the other hand, the decrease (in absolute value) in the elastic strains of grains oriented with the $\{10\bar{1}1\}$ and $\{10\bar{1}2\}$ grains perpendicular to the compression axis is accompanied by the increase (in absolute value) in the elastic strains of the 14H LPSO-phase, as measured during the tensile test. However, above 320 MPa, it is not possible to fit this diffraction peak because the substantial increase in the intensity of the $\{0002\}$ peak overlaps the 14H LPSO-phase peak.

The behavior of the elastic strains of grains oriented with their $\{11\bar{2}0\}$ planes perpendicular to the compression axis is similar to that seen in grains oriented with $\{10\bar{1}0\}$ planes perpendicular to the compression axis. After yielding, the evolution of the elastic strain remains almost linear or asymptotic. The later will imply that these grains are deforming plastically, as in the tension test.

Finally, the $\{0002\}$ diffraction peak can be fitted, especially after yield, where its intensity increases continuously (see Figure 8b). The increase in the $\{0002\}$ diffraction peak is caused by the activation of tensile twinning in non-DRXed grains. After yielding, the elastic strain of twins decreases (in absolute value) from 6620 μ strains at 302 MPa to 5352 μ

strains at 320 MPa. Above this applied stress, elastic strain of twins increases (in absolute terms) much faster than seen in the elastic behavior up to 12,470 μ strains at 459 MPa.

Figure 9 shows the bright field images of the extruded samples tested in compression (Figure 9a,b) and tension (Figure 9c) up to the level of 2% of plastic deformation in the zone axis of $B = [11\bar{2}0]$. Under compression, it is possible to observe the presence of tensile twin in highly oriented non-DRXed grains, which induces a rotation of almost 90° with respect to the parent grain, as was reported in the in situ tests under compression. Twins are very thin, and can pass among the lamellae presented in these grains. At the same time, twins are not observed crossing across the complete grain diameter, since they are temporarily pinned in thick γ precipitates. Twins are not observed in DRXed grains, where a high dislocation density is generated. Under tension, no twins were observed in either non-DRX or DRXed grains. A high dislocation density was observed in between the lamellar precipitates.

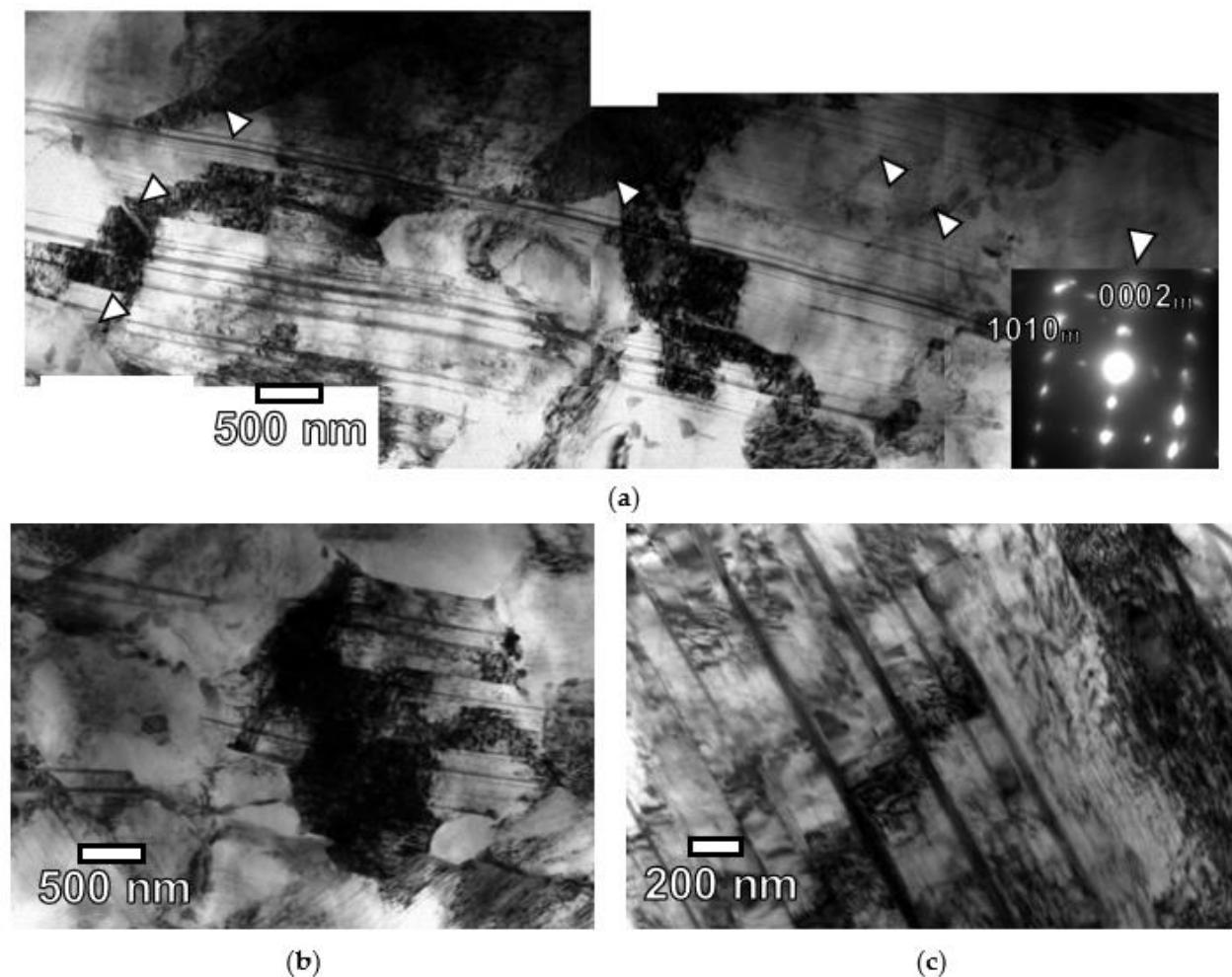


Figure 9. (a) Bright field image of a non-DRXed grain at the zone axis $B = [11\bar{2}0]$, deformed 2% from plastic strain under compression. (b) Bright field image of a DRXed grain at the zone axis $B = [11\bar{2}0]$ deformed 2% from plastic strain under compression. (c) Bright field image of a non-DRXed grain at the zone axis $B = [11\bar{2}0]$ deformed 2% from plastic strain under tension.

4. Discussion

The microstructure of the extruded alloy exhibits a bimodal grain structure consisting of randomly oriented fine DRXed grains and non-DRXed grains, highly oriented, with their basal planes parallel to the extrusion direction. The volume fraction of non-DRXed grains measured in the alloy is lower (around 30% of volume fraction [30], using the same processing parameters) than that reported in $Mg_{97}Y_2Zn_1$ with similar volume fraction,

without the presence of the lamellar structure within the magnesium grains. It seems that lamellar precipitates facilitate the nucleation of DRXed grains at their interfaces.

The relative crystal orientation of both types of grains controls the activation of the different deformation systems of magnesium. The non-DRXed grains have their basal planes parallel to the tensile or compressive axis. Therefore, the activation of the basal slip system is inhibited in these grains. On the other hand, the activation of tensile twinning is activated only under compression. The crystal lattice is reoriented within twins, where the basal plane rotates 86° with the initial orientation. Therefore, the intensity of the (0002) diffraction peak increases when tensile twinning begins. Under tension, these grains cannot deform plastically and they behave in a purely elastic manner until the fracture. It would be expected that the presence of highly oriented non-DRXed grains would induce a strong tension–compression asymmetry in magnesium. However, the yield stress values are equal in both cases, and the tensile and compressive curves are similar up to the point of 3% plastic strain. Yang et al. [20] also reported, in an alloy with a similar composition but with a grain structure characterized mainly by highly oriented non-DRXed grains, the same tensile and compressive behavior at the beginning of the curve. They proposed that LPSO plates generated at the basal plane effectively impede both the dislocation motion and the twinning activity. It is interesting to note that in this study, the compression curve (from yield stress to 3% of plastic deformation) is slightly higher, compared to the tensile curve. The main microstructural difference, compared to the study of Yang et al., is the presence of dense LPSO phase observed in this study. We have previously observed that LPSO fiber induces a higher mechanical strength in the alloy, which increases with the increase in the volume fraction of the LPSO phase.

The randomly oriented DRXed grains are favorably oriented for the activation of the slip of $\langle a \rangle$ dislocation along the basal slip. Therefore, grains oriented with the $\{10\bar{1}1\}$ and $\{10\bar{1}2\}$ planes perpendicular to the tensile or compressive axes lose their linearity only at the point of macroscopic yield stress. Therefore, independently of the stress mode, the beginning of plastic deformation is controlled by the DRXed grains. Since the beginning of the macroscopic plastic deformation is controlled by the activation of the basal slip in the DRXed sample, no differences would be expected between yield stress under tension and compression at the beginning of the test. However, when twinning is activated in non-DRXed grains, the applied stress and work-hardening in the compression tests increase (around 3% of plastic strain). TEM observation demonstrated that twinning was active at 2% plastic deformation. At the same time, twins are extremely thin, due to the presence of lamellar-shape precipitates that delay their coalescence and growth. Yang et al. [18] have shown that LPSO plates plastically deform when they are engulfed by the twins, explaining the delay of the process of the coalescence and growth of twins.

During the initial state of plastic deformation, DRXed grains oriented with the $\{10\bar{1}1\}$ and $\{10\bar{1}2\}$ planes perpendicular to the loading direction undergo a strong relaxation once the alloy yields. Since this strain difference, measured using Equation (1), is purely elastic, the relaxation stress could be grossly estimated using the Young Modulus for the planes obtained from the slope of the internal strain as a function of the applied stress in the elastic zone ($\Delta\sigma = E(hkil) \times \Delta\varepsilon_{\text{elas}}$). The relaxation stresses in grains with $\{10\bar{1}1\}$ and $\{10\bar{1}2\}$ planes perpendicular to the loading axis after yield stress are listed in Table 1. These stresses should be borne by stiff phases, i.e., the LPSO phase, or other magnesium grains whose crystallographic orientation inhibits the activation of dislocation slip or twinning system (“hard grains” [39]). The LPSO phase exhibits a higher Young Modulus (around 55 MPa) compared to that of the magnesium phase [40,41]. The relaxed stresses are higher in the tension test than in the compression, indicating that non-DRXed grains behave as a reinforcing phase only in tension tests.

Finally, it is interesting to note that from the point of view of the design of these alloys, both kinds of LPSO phases (LPSO lamellar-shape precipitates within magnesium grains and LPSO fiber at grain boundaries) are contributing to the reinforcement of the magnesium phase, although in two different ways. While the LPSO lamellar-shape precipitate show

a high level of interaction with dislocations and twins within the magnesium grains, the LPSO fibers assumed an additional stress transferred by the magnesium phase.

Table 1. Internal strains and relaxed stresses at the beginning of macroscopic yield stress in the tensile and compression tests.

Plane	Internal Strains (μ Strains)	Stress (MPa)	Internal Strains (μ Strains)	Stress (MPa)
	Tension		Compression	
$\{10\bar{1}1\}$	2033	87	1707	73
$\{10\bar{1}2\}$	3057	131	2501	108

5. Conclusions

The evolution of the internal strains during in situ tension and compression tests has been measured in the extruded Mg₉₇Gd₂Zn₁ alloy containing Long-Period Stacking Ordered (LPSO) phase and a lamellar structure within the magnesium phase, using synchrotron diffraction radiation. The following conclusions can be drawn:

- (1) The presence of the lamellar-shape precipitates within the Mg phase before the high temperature extrusion process promotes the recrystallization process due to the nucleation of fine equiaxed grains at the interface between the magnesium matrix and the lamellar-shape precipitates.
- (2) The macroscopic yielding is controlled by the activation of the basal slip systems in the DRXed grains, leading to a low tension–compression asymmetry. During the onset of the plastic regime, these grains can release a significant part of the assumed stress, since they can transfer part of it towards hard phases.
- (3) The elasto-plastic behavior of non-DRXed grains depends on the stress mode, tension and compression. Thus, these grains act as a reinforcing phase during tensile testing. Under compression, the activation of tensile twinning is activated. The presence of lamellar-shape precipitates delays the propagation of lenticular thin twins through the non-DRXed grains.

Author Contributions: Conceptualization, G.G. and P.P.; Methodology, G.G., J.M., P.P., R.B., H.L., S.K.K., E.M., N.S. and P.A.; Formal analysis, G.G. and J.M.; Investigation, G.G., J.M., P.P., R.B., H.L., S.K.K., E.M., N.S. and P.A.; Resources, H.L. and S.K.K.; Writing—original draft, G.G. and P.P.; Writing—review and editing, G.G., J.M., P.P., R.B., H.L., S.K.K., E.M., N.S. and P.A.; Funding acquisition, G.G. and P.A. All authors have read and agreed to the published version of the manuscript.

Funding: This research was funded by the Spanish Ministry of Science, Innovation and Universities, grant number TED2021-129580B-I00.

Data Availability Statement: The data presented in this study are available in this article.

Acknowledgments: Authors would like to acknowledge the Electron Microscopy Laboratory of CENIM-CSIC. The DeutchesElektronen-Synchrotron DESY is also acknowledged for the provision of beamtime at the P07B beamline of the Petra III synchrotron facility.

Conflicts of Interest: The authors declare no conflicts of interest. The funders had no role in the design of the study; in the collection, analyses, or interpretation of data; in the writing of the manuscript; or in the decision to publish the results.

References

1. Inoue, A.; Kawamura, Y.; Matsushita, M.; Hayashi, K.; Koike, J. Novel hexagonal structure and ultrahigh strength of magnesium solid solution in the Mg-Zn-Y system. *J. Mater. Res.* **2001**, *16*, 1894–1900. [[CrossRef](#)]
2. Yamasaki, M.; Hashimoto, K.; Hagihara, K.; Kawamura, Y. Effect of multimodal microstructure evolution on mechanical properties of Mg-Zn-Y extruded alloy. *Acta Mater.* **2011**, *59*, 3646–3658. [[CrossRef](#)]
3. Xua, D.; Hana, E.H.; Xua, Y. Effect of long-period stacking ordered phase on microstructure, mechanical property and corrosion resistance of Mg alloys: A review. *Prog. Nat. Sci. Mater. Inter.* **2016**, *26*, 117–128. [[CrossRef](#)]

4. Hagihara, K.; Kinoshita, A.; Sugino, Y.; Yamasaki, M.; Kawamura, Y.; Yasuda, H.Y. Effect of long-period stacking ordered phase on mechanical properties of Mg97Zn1Y2 extruded alloy. *Acta Mater.* **2010**, *58*, 6282–6292. [[CrossRef](#)]
5. Yiwen, C.; Jingya, W.; Weisen, Z.; Quan, L.; Mingdi, Y.; Tao, Y.; Xiaoqin, Z. CALPHAD-guided design of Mg-Y-Al alloy with improved strength and ductility via regulating the LPSO phase. *Acta Mater.* **2024**, *263*, 119521.
6. Itoi, T.; Seimiya, T.; Kawamura, Y.; Hirohashi, M. Long period stacking structures observed in Mg97Zn1Y2 alloy. *Scr. Mater.* **2004**, *51*, 107–111. [[CrossRef](#)]
7. Kawamura, Y.; Yamasaki, M. Formation and Mechanical Properties of Mg97Zn1RE2 Alloys with Long-Period Stacking Ordered Structure. *Mater. Trans.* **2007**, *48*, 2986–2992. [[CrossRef](#)]
8. Ding, S.J.; Xu, L.D.; Cai, X.C.; Gu, S.X.Y.; Wen, K.K.; Yu, H.; Chen, Z.; Sun, B.R.; Xin, S.W.; Shen, T.D. Exceptional thermal stability of ultrafine-grained long-period stacking ordered Mg alloy. *Rare Met.* **2022**, *41*, 1537–1542. [[CrossRef](#)]
9. Harjo, S.; Gong, W.; Aizawa, K.; Kawasaki, T.; Yamasaki, M. Strengthening of α Mg and long-period stacking ordered phases in a Mg-Zn-Y alloy by hot-extrusion with low extrusion ratio. *Acta Mater.* **2023**, *255*, 119029. [[CrossRef](#)]
10. Tokuzumi, T.; Mitsuhara, M.; Yamasaki, S.; Inamura, T.; Fujii, T.; Nakashima, H. Role of disclinations around kink bands on deformation behavior in Mg-Zn-Y alloys with a long-period stacking ordered phase. *Acta Mater.* **2023**, *248*, 118785. [[CrossRef](#)]
11. Yamasaki, M.; Anan, T.; Yoshimoto, S.; Kawamura, Y. Mechanical properties of warm-extruded Mg-Zn-Gd alloy with coherent 14H long periodic stacking ordered structure precipitate. *Scr. Mater.* **2005**, *53*, 799–803. [[CrossRef](#)]
12. Chen, B.; Lin, D.L.; Zeng, X.Q.; Lu, C. Microstructure and mechanical properties of ultrafine grained Mg97Y2Zn1 alloy processed by equal channel angular pressing. *J. Alloys Compd.* **2007**, *440*, 94–100. [[CrossRef](#)]
13. Yamasaki, M.; Sasaki, M.; Nishijima, M.; Hiraga, K.; Kawamura, Y. Formation of 14H long period stacking ordered structure and profuse stacking faults in Mg-Zn-Gd alloys during isothermal aging at high temperature. *Acta Mater.* **2007**, *55*, 6798–6805. [[CrossRef](#)]
14. Nie, J.F.; Oh-ishi, K.; Gao, X.; Hono, K. Solute segregation and precipitation in a creep-resistant Mg-Gd-Zn alloy. *Acta Mater.* **2008**, *56*, 6061–6076. [[CrossRef](#)]
15. Chun, Y.B.; Geng, J.; Stanford, N.; Davies, C.H.J.; Nie, J.F.; Barnett, M.R. Processing and properties of Mg-6Gd-1Zn-0.6Zr: Part 1—Recrystallisation and texture development. *Mat. Sci. Eng. A* **2011**, *528*, 3653–3658. [[CrossRef](#)]
16. Geng, J.; Chun, Y.B.; Stanford, N.; Davies, C.H.J.; Nie, J.F.; Barnett, M.R. Processing and properties of Mg-6Gd-1Zn-0.6Zr: Part 2. Mechanical properties and particle twin interactions. *Mat. Sci. Eng. A* **2011**, *528*, 3659–3665. [[CrossRef](#)]
17. Sato, K.; Tashiro, S.; Matsunaga, S.; Yamaguchi, Y.; Kiguchi, T.; Konno, T.J. Evolution of long-period stacking order (LPSO) in Mg97Zn1Gd2 cast alloys viewed by HAADF-STEM multi-scale electron tomography. *Phil. Mag.* **2018**, *98*, 1945–1960. [[CrossRef](#)]
18. Yang, Q.; Lv, S.; Yan, Z.; Yan, Z.; Hua, X.; Qui, X.; Meng, J. Nano-steps in long-period stacking ordered structures for ductility asymmetry of a strong-textured Mg-Gd-Zn alloy. *Mater. Des.* **2021**, *201*, 109482. [[CrossRef](#)]
19. Nishijima, M.; Hiraga, K.; Yamasaki, M.; Kawamura, Y. Characterization of β' Phase Precipitates in an Mg-5 at%Gd Alloy Aged in a Peak Hardness Condition, Studied by High-Angle Annular Detector Dark-Field Scanning Transmission Electron Microscopy. *Mater. Trans.* **2006**, *47*, 2109–2112. [[CrossRef](#)]
20. Li, Q.; Song, J.; Chen, Y.; Zhang, Q.; Zhu, Q.; Liu, Y.; Wang, J.; Zeng, X. In-situ TEM characterization of basal dislocations between nano-spaced long-period stacking ordered phases in MgYZn alloy. *Scr. Mater.* **2023**, *235*, 115601. [[CrossRef](#)]
21. Garces, G.; Máthis, K.; Barea, R.; Medina, J.; Pérez, P.; Stark, A.; Schell, N.; Adeva, P. Effect of precipitation in the compressive behavior of high strength Mg-Gd-Y-Zn extruded alloy. *Mat. Sci. Eng. A* **2019**, *768*, 138452. [[CrossRef](#)]
22. Ji, Z.K.; Qiao, X.G.; Yuan, L.; Cong, F.G.; Wang, G.J.; Zheng, M.Y. Exceptional fracture toughness in a high-strength Mg alloy with the synergetic effects of bimodal structure, LPSO, and nanoprecipitates. *Scr. Mater.* **2023**, *236*, 115675. [[CrossRef](#)]
23. Li, J.; Wang, F.; Zeng, J.; Zhao, C.; Jin, L.; Dong, J. Effect of the interspacing of intragranular lamellar LPSO phase on dynamic recrystallization behaviors of Mg-Gd-Y-Zn-Zr alloys. *Mater. Char.* **2022**, *193*, 112326. [[CrossRef](#)]
24. Su, N.; Deng, Q.; Wu, Y.; Peng, L.; Yang, K.; Chen, Q. Deformation-induced dissolution of long-period stacking ordered structures and its re-precipitation in a Mg-Gd-Zn-Mn alloy. *Mater. Char.* **2021**, *171*, 110756. [[CrossRef](#)]
25. Schmidt, J.; Beyerlein, I.J.; Knezevic, M.; Reimers, W. Adjustment of the Mechanical Properties of Mg2Nd and Mg2Yb by Optimizing Their Microstructures. *Metals* **2021**, *11*, 377. [[CrossRef](#)]
26. Frydrych, K.; Libura, T.; Kowalewski, Z.; Maj, M.; Kowalczyk-Gajewska, K. On the role of slip, twinning and detwinning in magnesium alloy AZ31B sheet. *Mater. Sci. Eng. A* **2021**, *813*, 141152. [[CrossRef](#)]
27. Huang, X.; Xin, Y.; Cao, Y.; Huang, G.; Li, W. A quantitative study on planar mechanical anisotropy of a Mg-2Zn-1Ca alloy. *J. Mater. Sci. Technol.* **2022**, *109*, 30. [[CrossRef](#)]
28. Xu, J.; Guan, B.; Xin, Y.; Wei, X.; Huang, G.; Liu, C. A weak texture dependence of Hall–Petch relation in a rare-earth containing magnesium alloy. *J. Mater. Sci. Technol.* **2021**, *99*, 251. [[CrossRef](#)]
29. Kleiner, S.; Uggowitzer, P.J. Mechanical anisotropy of extruded Mg-6% Al-1% Zn alloy. *Mat. Sci. Eng. A* **2004**, *379*, 258. [[CrossRef](#)]
30. Garces, G.; Medina, J.; Perez, P.; Stark, A.; Lim, H.K.; Kim, S.; Schell, N.; Adeva, P. Analysis of the Microstructure Role in the Yield Asymmetry of Extruded Mg-LPSO Alloys Using In Situ Diffraction Experiments. *JOM* **2022**, *74*, 2609–2621. [[CrossRef](#)]
31. Schindelin, J.; Arganda-Carreras, I.; Frise, E.; Kaynig, V.; Longair, M.; Pietzsch, T.; Preibisch, S.; Rueden, C.; Saalfeld, S.; Schmid, B.; et al. Fiji: An open-source platform for biological-image analysis. *Nat. Methods* **2012**, *9*, 676–682. [[CrossRef](#)] [[PubMed](#)]
32. Zhou, X.; Ha, C.; Yi, S.; Bohlen, J.; Schell, N.; Chi, Y.; Zheng, M.; Brokmeier, H.G. Texture and Lattice Strain Evolution during Tensile Loading of Mg-Zn Alloys Measured by Synchrotron Diffraction. *Metals* **2020**, *10*, 124. [[CrossRef](#)]

33. Lutterotti, L.; Bortolotti, M.; Ischia, G.; Lonardelli, I.; Wenk, H.R. Rietveld Texture Analysis from Diffraction Images. *Z. Krist. Suppl.* **2007**, *1*, 125–130. [[CrossRef](#)]
34. Schindelin, J.; Rueden, C.T.; Hiner, M.C.; Eliceiri, K.W. The ImageJ ecosystem: An open platform for biomedical image analysis. *Mol. Reprod. Dev.* **2015**, *82*, 518–529. [[CrossRef](#)] [[PubMed](#)]
35. Lutterotti, L.; Matthies, S.; Wenk, H.R.; Schultz, A.S.; Richardson, J.W. Combined texture and structure analysis of deformed limestone from time-of-flight neutron diffraction spectra. *J. Appl. Phys.* **1997**, *81*, 594–600. [[CrossRef](#)]
36. Egusa, D.; Abe, E. The structure of long period stacking/order Mg-Zn-RE phases with extended non-stoichiometry ranges. *Acta Mater.* **2012**, *60*, 166–178. [[CrossRef](#)]
37. Agnew, S.R.; Mulay, R.P.; Polesak, F.J., III; Calhoun, C.A.; Bhattacharyya, J.J.; Clausen, B. In situ neutron diffraction and polycrystal plasticity modeling of a Mg-Y-Nd-Zr alloy: Effects of precipitation on individual deformation mechanisms. *Acta Mater.* **2013**, *61*, 3769–3780. [[CrossRef](#)]
38. Zhu, Y.M.; Morton, A.J.; Nie, J.F. The 18R and 14H long-period stacking ordered structures in Mg-Y-Zn alloys. *Acta Mater.* **2010**, *58*, 2936–2947. [[CrossRef](#)]
39. Agnew, S.R.; Brown, D.W.; Tome, C.N. Validating a polycrystal model for the elastoplastic response of magnesium alloy AZ31 using in situ neutron diffraction. *Acta Mater.* **2006**, *54*, 4841–4852. [[CrossRef](#)]
40. Tane, M.; Nagai, Y.; Kimizuka, H.; Hagihara, K.; Kawamura, Y. Elastic properties of an Mg-Zn-Y alloy single crystal with a long-period stacking-ordered structure. *Acta Mater.* **2013**, *61*, 6338–6351. [[CrossRef](#)]
41. Tane, M.; Kimizuka, H.; Hagihara, K.; Suzuki, S.; Mayama, T.; Sekino, T.; Nagai, Y. Effects of stacking sequence and short-range ordering of solute atoms on elastic properties of Mg-Zn-Y alloys with long-period stacking ordered structures. *Acta Mater.* **2015**, *96*, 170–188. [[CrossRef](#)]

Disclaimer/Publisher’s Note: The statements, opinions and data contained in all publications are solely those of the individual author(s) and contributor(s) and not of MDPI and/or the editor(s). MDPI and/or the editor(s) disclaim responsibility for any injury to people or property resulting from any ideas, methods, instructions or products referred to in the content.